Monthly Notices
of the
ROYAL ASTRONOMICAL SOCIETY

MNRAS **462,** 167–180 (2016)
Advance Access publication 2016 July 8

doi:10.1093/mnras/stw1651

Characterizing strong lensing galaxy clusters using the Millennium-XXL and MOKA simulations

Carlo Giocoli,[1⋆] Mario Bonamigo,[1] Marceau Limousin,[1] Massimo Meneghetti,[2,3] Lauro Moscardini,[4,2,3] Raul E. Angulo,[5] Giulia Despali[1,6] and Eric Jullo[1]

[1]*Aix Marseille Université, CNRS, LAM (Laboratoire d'Astrophysique de Marseille) UMR 7326, F-13388 Marseille, France*
[2]*INAF - Osservatorio Astronomico di Bologna, via Ranzani 1, I-40127 Bologna, Italy*
[3]*INFN - Sezione di Bologna, viale Berti Pichat 6/2, I-40127 Bologna, Italy*
[4]*Dipartimento di Fisica e Astronomia, Alma Mater Studiorum Università di Bologna, viale Berti Pichat, 6/2, I-40127 Bologna, Italy*
[5]*Centro de Estudios de Física del Cosmos de Aragón (CEFCA), Plaza San Juan 1, Planta-2, E-44001 Teruel, Spain*
[6]*Max Planck Institute for Astrophysics, Karl-Schwarzschild-Strasse 1, D-85740 Garching, Germany*

Accepted 2016 July 5. Received 2016 July 5; in original form 2016 April 11

ABSTRACT

In this paper, we investigate the strong lensing statistics in galaxyclusters. We extract dark matter haloes from the Millennium-XXL simulation, compute their *Einstein* radius distribution, and find a very good agreement with Monte Carlo predictions produced with the MOKA code. The distribution of the *Einstein* radii is well described by a lognormal distribution, with a considerable fraction of the largest systems boosted by different projection effects. We discuss the importance of substructures and triaxiality in shaping the size of the critical lines for cluster size haloes. We then model and interpret the different deviations, accounting for the presence of a Brightest Central Galaxy (BCG) and two different stellar mass density profiles. We present scaling relations between weak lensing quantities and the size of the *Einstein* radii. Finally, we discuss how sensible is the distribution of the *Einstein* radii on the cosmological parameters $\Omega_{\rm M} - \sigma_8$ finding that cosmologies with higher $\Omega_{\rm M}$ and σ_8 possess a large sample of strong lensing clusters. The *Einstein* radius distribution may help distinguish Planck13 and *WMAP*7 cosmology at 3σ.

Key words: gravitational lensing: strong – methods: numerical.

1 INTRODUCTION

Spectroscopic galaxy redshift surveys and numerical *N*-body simulations have revealed a large-scale distribution of matter in the Universe featuring a complex network of interconnected filamentary galaxy associations (Tormen, Moscardini & Yoshida 2004; Springel et al. 2005; The Dark Energy Survey Collaboration 2005; Sousbie et al. 2008; Sousbie, Pichon & Kawahara 2011; Guzzo et al. 2014; Percival et al. 2014; Codis, Pichon & Pogosyan 2015; Le Fèvre et al. 2015). Vertices, i.e. interconnections among the filaments, correspond to the very dense compact nodes within this *cosmic web* where one can find massive galaxy clusters (Bryan & Norman 1998; Tormen 1998; Shaw et al. 2006; Bellagamba et al. 2011; Borgani & Kravtsov 2011).

The mass density distribution in clusters can be inferred using different wavelength observations (Meneghetti et al. 2010a; Donnarumma et al. 2011; Donahue et al. 2016). In particular, optical and near-infrared data provided by, for instance, the Subaru and the *Hubble Space telescopes* (*HST*) are allowing us to indirectly infer the total projected matter density distribution in clusters through its effect of gravitationally bending the light of background galaxies (Jullo et al. 2007; Limousin et al. 2016; Merten et al. 2015). Gravitational lensing, as predicted by the *Einstein*'s General Relativity, deflects light-rays once they get close to a deep potential well (Einstein 1918; Landau & Lifshitz 1971). Light-rays from distant galaxies travelling in the space–time of our Universe can be weakly or strongly bent when they approach a galaxy cluster (Bartelmann & Schneider 2001; Bartelmann 2010). The weak lensing regime happens when the light-rays travel far from the centre of the cluster. In this case, the shapes of background galaxies are only slightly altered and, for a good determination of the signal, it is usually necessary to average over a large sample of background systems (Hoekstra et al. 2012, 2013; Giocoli et al. 2014; Radovich et al. 2015; Formicola et al. 2016). The strong lensing (SL) regime takes place when the light-rays transit close to the centre of the cluster, and the mass density becomes critical: the lensing event in this case is non-linear and images of background galaxies may be multiplied and/or appear stretched and elongated. Depending on the quality of the data and on their availability, weak and SL data can be used

⋆ E-mail: cgiocoli@gmail.com.

separately or jointly for a better reconstruction of the projected mass from the very central region to the outskirts of the cluster. In the following, we will concentrate on the SL regime and on the objects that originate it, which we will refer to as strong lensing clusters (SLCs).

SLCs may constitute a peculiar class of objects. While their existence is a natural consequence of General Relativity, 'giant arcs' – extremely distorted images of background galaxies – hosted in clusters have been discovered only 30 yr ago in the core of Abell 370, independently by Lynds & Petrosian (1986) and Soucail et al. (1987). This observation was recognized by Paczynski (1987) as the result of strong gravitational lensing, a hypothesis later confirmed by the measurement of the redshift of the arc (Soucail et al. 1988a,b).

Since then, SLCs have led to many important advances in cosmology: (i) being a direct and precise probe of the two-dimensional projected mass density, SL has provided accurate mass maps, constraining structure formation properties and evolution scenarios (for example: Broadhurst et al. 2000; Sand, Treu & Ellis 2002; Bradač et al. 2006; Saha & Williams 2006; Zitrin & Broadhurst 2009; Zitrin et al. 2009; Newman et al. 2011; Verdugo et al. 2011; Sharon et al. 2014); (ii) producing a natural gravitational amplification, SL has allowed us to push the frontier of our telescopes (for example: Richard et al. 2006; Coe et al. 2013; Atek et al. 2014; Zitrin et al. 2014); (iii) providing a method to probe the dark energy equation of state, since images position depends on the underling cosmology (for example: Soucail, Kneib & Golse 2004; Jullo et al. 2010).

SLCs are now well established as a promising class of objects that cannot be ignored in cosmology, and their future is extremely promising, since future facilities are expected to detect thousands of SLCs (Laureijs et al. 2011; Boldrin et al. 2012, 2016; Serjeant 2014), and the exquisite resolution of the *James Webb Space Telescope* (*JWST*) will deliver unique multicolour data sets for some of them. The growing importance of SLCs has been recently illustrated by the CLASH programme (Postman et al. 2012) which has been awarded of 500 *HST* orbits to observe 25 massive SLCs. More recently, the Hubble Deep Fields Initiative has unanimously recommended a 'Frontier Field' programme of six deep fields concentrated on SL clusters (together with six deep 'blank fields') in order to advance our knowledge of the early epochs of galaxy formation and to eventually offer a glimpse of *JWST*'s universe (http://www.stsci.edu/hst/campaigns/frontier-fields). Each cluster will be imaged with 140 orbits, leading to a total of 840 orbits dedicated to the Frontier Field Initiative.

Very encouraging is also the work performed by Zitrin et al. (2012) on reconstructing the mass density distribution and the *Einstein* radius (which estimates the size of the SL region) of a large sample of SDSS clusters. In this case, the 'blind' approach based on the assumption that light traces mass has allowed us to establish that the *Einstein* radius distribution of clusters with $0.1 < z_l < 0.55$ has a lognormal shape. Furthermore, a visual inspection has revealed that approximately 20 per cent of SLCs are boosted by various projection effects.

Given the significance of SLCs, characterizing this peculiar class of object is crucial and this has been the focus of many studies (for example: Hennawi et al. 2007; Meneghetti et al. 2010b; Redlich et al. 2012; Waizmann, Redlich & Bartelmann 2012). This is also the motivation of this work, where we aim at characterizing which clusters do generate SL features. Our approach is twofold: (i) first, we will use the large sample of cluster statistics afforded by the Millennium-XXL simulation (M-XXL; Angulo et al. 2012) – exploiting its large size (3 Gpc h^{-1} box side), that allows us to follow the formation of many massive haloes; (ii) secondly, we will complement the statistics with a cosmological study based on clusters modelled using the MOKA code (Giocoli et al. 2012a).

We want to spend few words about the fact that the *Einstein* radius of lenses is not a direct observable quantity. The *Einstein* radius, defined by the location of the tangential critical lines (more will be discussed about this in the first section) is a byproduct of the mass reconstruction pipeline by mean of parametric algorithms that typically assume that mass traces the light (Jullo et al. 2007; Zitrin et al. 2011) or adaptively reconstruct the mass density distribution using non-parametric approaches (Merten 2014).

The paper is organized as follows: in Section 2, we present the numerical simulations and the pseudo-analytical methods we adopt as bases for our analyses; in Section 3, we discuss the scaling relations between the size of the *Einstein* radius and weak lensing-derived quantities; in Section 4, we present how the *Einstein* radius distribution depends on the matter content of the universe and on the initial normalization of the power spectrum. Finally in Section 5, we summarize and discuss our results.

2 METHODS

In this paper, we aim at studying the SL properties of galaxy clusters – through the size of their *Einstein* radius – extracted from a very large cosmological box. However, the limitation of possessing the simulation only for one cosmological model in addition to the fact that the run has been performed only using collisionless dark matter (DM) particles forced us to complement the analyses using a pseudo-analytic approach to simulate convergence maps of triaxial clusters. This latter method allows us, in a more flexible way, to investigate which properties of clusters mainly contribute in shaping the *Einstein* radius, to quantify the contribution of the stellar component and to understand how the *Einstein* radius distribution of clusters may depend on specific cosmological parameters.

2.1 SL of clusters in the M-XXL simulation

With a box side of 3 Gpc h^{-1}, the M-XXL simulation (Angulo et al. 2012) was especially tailored to study massive haloes which can be only found in very large volumes, because of their nature of extremely rare objects. The $6720^3 \sim 3 \times 10^{11}$ DM particles have a mass of $6.174 \times 10^9\,\mathrm{M}_\odot\,h^{-1}$; the Plummer-equivalent softening length is $\epsilon = 13.7$ kpc. For reasons of consistency with the previous Millennium runs (Springel et al. 2005; Boylan-Kolchin et al. 2009), the adopted Λ cold dark matter cosmology as the following parameters total matter density $\Omega_\mathrm{M} = 0.25$, baryons density $\Omega_\mathrm{b} = 0.045$, cosmological constant $\Omega_\Lambda = 0.75$, power spectrum normalization $\sigma_8 = 0.9$ and dimensionless Hubble parameter in $H_0/100\,\mathrm{km\,s^{-1}\,Mpc^{-1}}\,h = 0.73$. We remind the reader that the simulated volume of the M-XXL is equivalent to the whole observable Universe up to redshift $z = 0.72$.

At each simulation snapshot, haloes have been identified using an Friends of Friends (FoF) algorithm. For each FoF-group, starting from the particle with the minimum potential, we then compute M_{200} as the mass enclosing a sphere 200 times denser than the critical density ρ_c at that redshift. In our analysis – for the motivation we will underline later – we will consider the halo catalogue at $z = 1$ and the corresponding snapshot files. Due to the large number of haloes identified in the simulation volume, we restrict our analysis only to the ones more massive than $3 \times 10^{14}\,\mathrm{M}_\odot\,h^{-1}$ – corresponding to 3135 systems. For each halo respecting this criterion, we store all the particles enclosed in a cube of $8\,\mathrm{Mpc}\,h^{-1}$ by side and project them in a 2D-mass map resolved with 2048×2048 pixels using the

Triangular Shape Cloud technique, along six different directions. In the first three cases, we consider three projections along the Cartesian axes, which are then *random* with respect to the cluster morphology, we then consider three *peculiar projections* i.e. along the ellipsoid axes as computed in Bonamigo et al. (2015): major, intermediate and minor axes. In placing the particles on the grid, to avoid particle noise effects (Rau, Vegetti & White 2013; Angulo et al. 2014) due to the discreteness of the DM density, we apply a Gaussian filter with a scale of 3.25 kpc h^{-1}, which corresponds to approximately one third of the simulation Plummer-equivalent softening.

From the constructed mass density maps $\Sigma(x_1, x_2)$ – where x_1 and x_2 are the two Cartesian coordinates on the 2D map projected in the plane of the sky – we compute the convergence $\kappa(x_1, x_2)$ as

$$\kappa(x_1, x_2) = \frac{\Sigma(x_1, x_2)}{\Sigma_{\rm crit}} \tag{1}$$

with

$$\Sigma_{\rm crit} \equiv \frac{c^2}{4\pi G}\frac{D_{\rm l}}{D_{\rm s}D_{\rm ls}} \equiv \frac{c^2}{4\pi G}\frac{1}{D_{\rm lens}}, \tag{2}$$

where c represents the speed of light and G the universal gravitational constant; $D_{\rm l}$, $D_{\rm s}$ and $D_{\rm ls}$ are the angular diameter distances between observer-lens, observer-source and source-lens, respectively; we also define the lensing distance $D_{\rm lens} \equiv D_{\rm ls}D_{\rm s}/D_{\rm l}$. We assume clusters to be located at $z_{\rm l} = 0.5$ and sources at $z_{\rm s} = 2.5$, computing the distances assuming the cosmological parameters in agreement with the Planck13 results (Planck Collaboration I 2014): the matter density parameter $\Omega_{\rm M} = 0.307$, the contribution of Λ $\Omega_\Lambda = 0.693$, the normalized Hubble constant $h = 0.6777$ and the normalization of the initial power spectrum $\sigma_8 = 0.829$. We do so because, even if the M-XXL simulation has been run with a different set of cosmological parameters, we assume to be able to rescale those clusters at $z = 1$ from an M-XXL cosmology to be a sample at $z = 0.5$ in a Planck13 cosmology. This is supported by the fact that the halo properties at $z = 1$ in the M-XXL cosmology are very similar to those at $z = 0.5$ in a Planck13 cosmology (Sheth & Tormen 1999; Macciò, Dutton & van den Bosch 2008; Zhao et al. 2009; Giocoli, Tormen & Sheth 2012b; Despali et al. 2016); even if the two mass functions for haloes more massive than $3 \times 10^{14}\,{\rm M}_\odot\,h^{-1}$ may be different by more than 50 per cent, the two concentration–mass relations deviate by less than 5 per cent. From the convergence, we can define the effective lensing potential as

$$\Phi(x_1, x_2) \equiv \frac{1}{\pi}\int \kappa(\boldsymbol{x}')\ln|\boldsymbol{x} - \boldsymbol{x}'|{\rm d}^2\boldsymbol{x}', \tag{3}$$

with $\boldsymbol{x} \equiv (x_1, x_2)$, and then the pseudo-vector field of the shear $\gamma = \gamma_1 + i\gamma_2$ as

$$\gamma_1(x_1, x_2) = \frac{1}{2}\left(\Phi_{11} - \Phi_{22}\right), \tag{4}$$

$$\gamma_2(x_1, x_2) = \Phi_{12} = \Phi_{21} \tag{5}$$

with Φ_{ij} representing the i and j derivatives of the effective lensing potential (Bartelmann & Schneider 2001; Bacon, Amara & Read 2010). At first order, gravitational lensing induces distortion and stretch on background sources: typically a circular source is mapped through gravitational lensing into an ellipse when both k and γ are different from zero. These effects are described by the Jacobian matrix:

$$\mathbf{A} = \begin{pmatrix} 1-\kappa-\gamma_1 & -\gamma_2 \\ -\gamma_2 & 1-\kappa+\gamma_1 \end{pmatrix}. \tag{6}$$

The magnification is quantified as the inverse determinant of the Jacobian matrix that can be read as

$$\mu \equiv \frac{1}{\det A} = \frac{1}{(1-\kappa)^2 - \gamma^2}; \tag{7}$$

the inverse of the eigenvalues of the Jacobian matrix measure the amplification in radial and tangential direction of background sources:

$$\mu_r = \frac{1}{1-\kappa+\gamma} \tag{8}$$

$$\mu_t = \frac{1}{1-\kappa-\gamma}. \tag{9}$$

For circularly symmetric lenses, the regions in the image plane where the denominator of the relations above is equal to zero define where the source images are infinitely radially and tangentially magnified, respectively. In particular images forming close to the tangential critical curve are strongly distorted tangentially to it.

The definition of critical curves is more complex and non-trivial in asymmetric, substructured and triaxial clusters. From each convergence map, the lensing potential and the shear are numerically computed in Fourier space[1] where derivatives are easily and efficiently calculated. To avoid artificial boundary effects, each map is enclosed in a zero-padded region of 1024 pixels. We have tested the impact of the size of the zero-padded regions on the weak and SL properties of individual non-periodic cluster maps and find that artefact mirror clusters do not appear when the size of the zero region is at least half of the considered field of view. To define the *Einstein* radius of the cluster, we identify in the cluster maps points of infinite tangential magnification $\theta_{\rm t}$ and define the *Einstein* radius $\theta_{\rm E}$ as the median distance of these points from the cluster centre:

$$\theta_{\rm E} \equiv {\rm med}\left\{\sqrt{\left(\theta_{i,x_1} - \theta_{{\rm c},x_1}\right)^2 + \left(\theta_{i,x_2} - \theta_{{\rm c},x_2}\right)^2}\;\middle|\;\theta_i \in \theta_{\rm t}\right\}. \tag{10}$$

We define the centre of the cluster $\theta_{\rm c}$ as the position of the particle with minimum potential and the connected region defined by the tangential critical points $\theta_{\rm t}$, when they exist, have to enclose the cluster centre; this ensures that the critical points are not eventually assigned to a substructure present in the field of view. The robustness of this definition has already been tested and discussed in a series of works (Meneghetti et al. 2008, 2010b; Redlich et al. 2012; Giocoli et al. 2014) to which we remind the reader for more details. The size of the *Einstein* radius defines a measure of the SL region and, for an axially symmetric lens, permits to estimate the mass enclosed within it using the equation:

$$\theta_{\rm E} = \left(\frac{4\,GM(<\theta_{\rm E})}{c^2}\frac{D_{\rm ls}}{D_{\rm l}D_{\rm s}}\right)^{1/2} \tag{11}$$

assuming that all mass is located at the centre of the lens. By geometrically measuring the area A enclosed by the tangential critical curve, it is possible to define the effective *Einstein* radius as $\theta_{\rm E,eff} = \sqrt{\mathbf{A}/\pi}$. However, we will rely on the median *Einstein* radius definition that – as noticed by Meneghetti et al. (2011) and Giocoli et al. (2014) – better captures the presence of asymmetries of the matter distribution towards the cluster centre.

In Fig. 1, we show the six considered projections of the halo in which one them has the largest *Einstein* radius (75 arcsec) in our constructed catalogue – namely in the bottom-left panel. The top panels show the x, y and z projections, while the bottom ones

[1] Using the FFTW libraries: http://www.fftw.org.

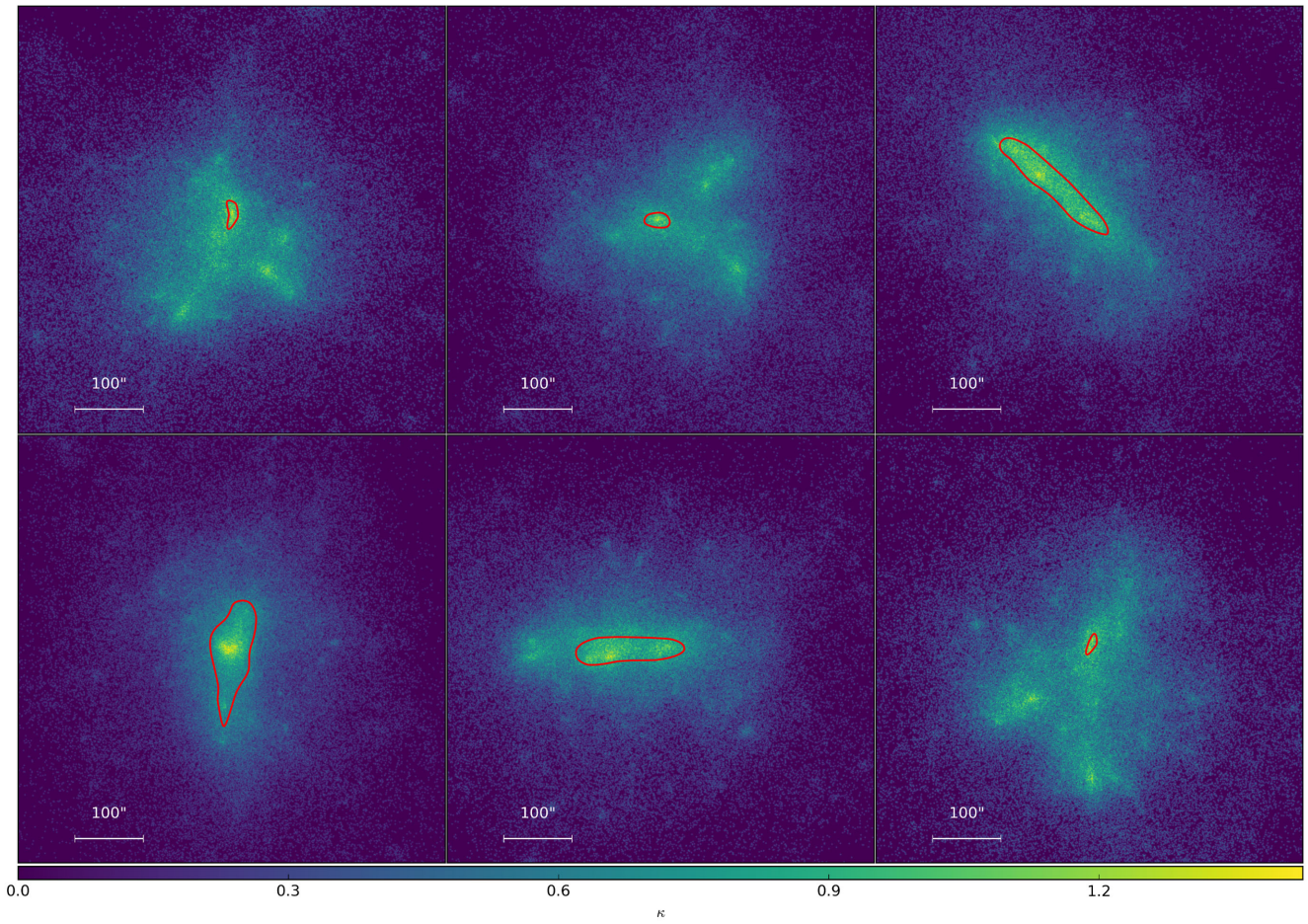

Figure 1. Convergence maps of different projections of a halo extracted from the M-XXL simulation with mass $M_{200} = 1.2 \times 10^{15}\,\mathrm{M}_{\odot}\,h^{-1}$. The red curves in each panel represent the tangential critical lines from which we compute the median *Einstein* radii. The top-three images show the three projections along the Cartesian axes (i.e. random with respect to the cluster morphology), while the bottom ones from left to right, are the projections along the major, intermediate and minor axes, respectively. This particular cluster has the peculiarity of having in one projection (namely the one in the left bottom panel) the largest *Einstein* radius in our sample: 75 arcsec.

the projections along the major, intermediate and minor axis of the halo ellipsoid, from left to right, respectively. In each panel, the red curves represent the tangential critical curves, i.e. where images of background galaxies would appear highly tangentially magnified if located close to the optical axis of the lens system. From the figure, we notice that the largest *Einstein* radius occurs, in this case – as in most of the cases, when the major axis of the cluster ellipsoid is oriented along the line of sight; the opposite holds when the minor axis points towards the observer.

From the measured *Einstein* radius of each of the six projections of all clusters in the M-XXL, we can summarize (as it can be read in Table 1) that in the *random projections* the probability of having the largest *Einstein* radius is uniform in the three cases as expected. However, considering the *peculiar projections* sample we notice that in 86 per cent of the cases the largest *Einstein* radius appears when the major axis of the ellipsoid is oriented along the line of sight and in 12 per cent (2 per cent) of the cases when the orientation is the intermediate (minor) axis. We have investigated those latter cases and they arise either (i) when there is a merging event which manifests in the presence of a massive substructure projected in correspondence of the cluster centre and/or (ii) when the cluster ellipsoid is very elongated in the plane of the sky.

Table 1. Percentage of the projections along which M-XXL clusters have the largest *Einstein* radius for the *random* and the *peculiar* projections, respectively.

Projection	per cent (*random*)
x	34 per cent
y	32 per cent
z	34 per cent
Projection	per cent (*peculiar*)
Major axis of the ellipsoid	86 per cent
Intermediate	12 per cent
Minor	2 per cent

In the left-hand panel of Fig. 2, we quantify by how much the *Einstein* radius grows when the cluster is oriented along the major axis of its mass ellipsoid. We consider all clusters having at least an *Einstein* radius of 7 arcsec along one of the considered projections.[2] In this case, we compare the size of the *Einstein* radius computed

[2] The value of 7 arcsec ensures that the measurement of the size of the *Einstein* radius of the cluster is not affected nor by particle noise neither by the finite grid size of the map.

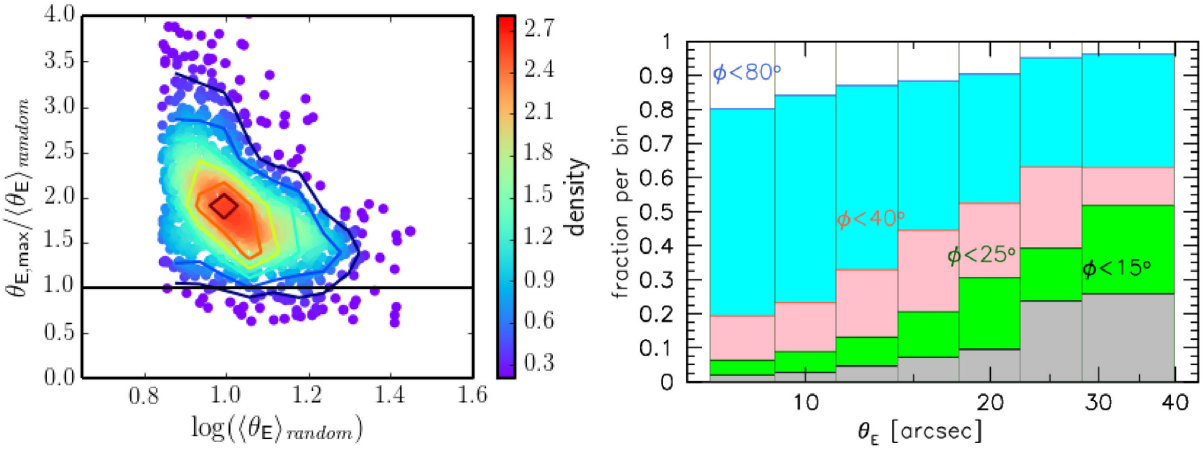

Figure 2. Left-hand panel: scatter plots of the relative size of the *Einstein* radii when the cluster major axis of the ellipsoid is oriented along the line of sight with compared to the average value of the three *random* projections: $\langle\theta_E\rangle_{random}$. Right-hand panel: fraction i of clusters with an angle ϕ between the direction of the major axis of the mass ellipsoid and the line of sight smaller than 80°, 40°, 25° and 10° as a function of the *Einstein* radius.

when the cluster is oriented along the major axis with respect to the average value measured from its three *random projections*. From the figure, we observe that the typical size of an *Einstein* radius may grow up to a factor of 2/3 when the cluster is aligned along the line of sight with respect to a random orientation; we also notice some cases where the *Einstein* radius computed in a *random projection* is larger than the value measured when the mass ellipsoid is oriented along the line of sight; as discussed previously we verified that those cases are merging clusters or very elongated ellipsoids in the plane of the sky. All this brings more light to the general picture that most of the SLCs may possess their DM halo major axis preferentially pointing close to the line of sight (Oguri & Blandford 2009). This is more evident in the right-hand panel of the same figure where we show the fraction of SLCs per different bins in θ_E that possess an angle ϕ between the major axis of the ellipsoid and the line of sight smaller than a given value: 65 per cent of SLCs with $30 < \theta_E < 40$ have an angle ϕ between the direction of their major axis and the line of sight smaller than 40°. Our finding are quite consistent with the results presented by Oguri et al. (2005) where the authors also discuss that the apparent steep observed mass profile can be reconciled with theoretical models if the triaxial ellipsoid of the DM halo is preferentially oriented with the major axis along the line of sight.

However, when looking at random projections in the plane of the sky, the sole effect of triaxiality is less obvious. Fig. 3 shows the difference that might arise in the distribution of shapes – namely minor to major axis ratio s – by selecting clusters that are strong lenses (blue histograms) instead of the general population (black histograms). Haloes have been subdivided in bins of *Einstein* radius θ_E, each shown in a different panel. Even though, as previously found by Hennawi et al. (2007), the distribution of the axis ratio of SLCs does not seem to differ from the distribution of the overall population, the mean values (vertical dashed lines) vary up to 5 per cent, in particular for very large θ_E. A Kolmogorov–Smirnov test showed that we can reject the hypothesis that the samples are taken from the same distribution at significance level of 10 per cent, meaning that there is a low probability that SLC have the same shape properties of the overall population. This suggests that the concentration is mainly responsible in driving the correlation of the cluster *Einstein* radii.

It is important to underline that the effect of correlated and uncorrelated large-scale structures may also impact the lensing properties

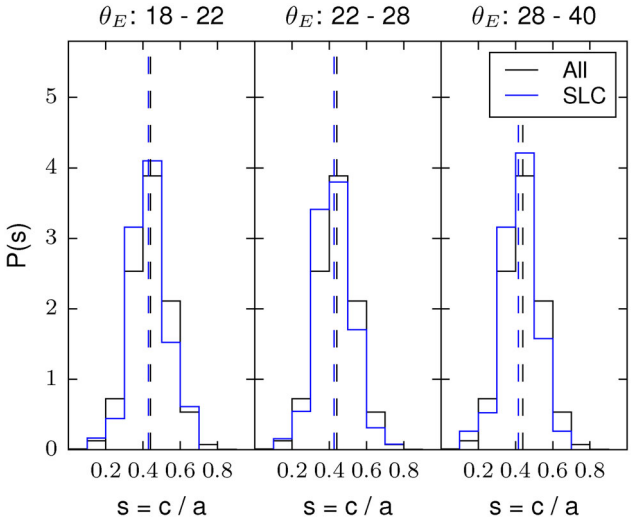

Figure 3. Probability distribution functions of the minor to major axis ratio of the overall M-XXL cluster population (black histogram) and of the SLCs (blue histogram), with each panel representing a different bin in θ_E. Vertical dashed lines indicate the mean of the corresponding sample.

of galaxy clusters and boost their SL cross-section as well as the size of the *Einstein* radius (Puchwein & Hilbert 2009). Usually to quantify the impact of uncorrelated structures along the line of sight, it is necessary to run expensive multiplane ray-tracing lensing simulations of clusters and matter extracted from cosmological runs (Hilbert et al. 2008; Petkova, Metcalf & Giocoli 2014; Giocoli et al. 2016), things that are beyond the purpose of this paper. However, the effect of correlated structures on the lensing properties can be studied selecting for each cluster projection a larger region along the line of sight, and quantify how these changes on the determination of the *Einstein* radius. To do so, we have produced two other sets of convergence maps, one selecting particles from a region of 16 Mpc h^{-1} and another from 32 Mpc h^{-1} along the line of sight, and projecting all of them into a single lens plane. We still keep the size of the region in the plane of the sky to be 8 Mcp h^{-1} of a side. As an example, in Fig. 4 we show the average convergence power spectra of the *random projections* sample

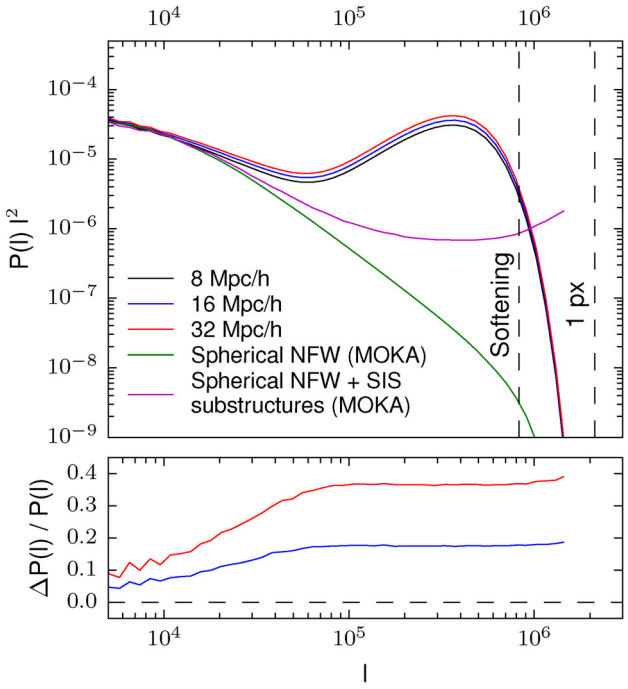

Figure 4. Average convergence power spectrum of haloes of the M-XXL simulation. Black, blue and red curve show the average power spectrum derived extracting the particles contained in a region of 8, 16 and 32 Mpc h^{-1} along the line of sight; in the plane of the sky in all three cases we have considered particles in a square of 8 Mpc h^{-1} of side. The green curve shows the prediction from smooth NFW spherical haloes, while the purple one presents the prediction for spherical MOKA haloes with substructures modelled with a SIS profile. The bottom panel shows the relative residuals of the average power spectra measured using 16 and 32 Mpc h^{-1} with respect to the one computed assuming 8 Mpc h^{-1} as box side along the line of sight.

considering a region of 8, 16 and 32 Mpc h^{-1} along the line of sight in black, blue and red, respectively. In the bottom panel, we present the relative residuals of the last two cases with respect to the 8 Mpc h^{-1} reference one. We notice that the inclusion of more matter along the line of sight tends to increase the convergence power spectrum at small scales of about 20 per cent for 16 Mpc h^{-1} and almost 40 per cent for 32 Mpc h^{-1}, which however contains four times the volume. In the figure, we show also for comparison the prediction from a smooth NFW halo (green curve) and the power spectrum of a spherical halo (with the same large-scale normalization) with substructures (in magenta): both curves are obtained by averaging produced using MOKA haloes (see below), with the same masses and NFW concentrations of the M-XXL sample. In this case, we observe that the presence of substructures in a halo tends to increase the small-scale power of more than one order of magnitude for $l \gtrsim 3 \times 10^4$ with respect to a smooth case. The other interesting behaviour is that while the power spectrum of haloes extracted from the M-XXL are characterized at small scales by the particle noise and finite grid size of the maps (Vale & White 2003), MOKA haloes are particle noise-free and the only numerical limitation at small scale is set by the desired grid size of the map.

Puchwein & Hilbert (2009) have shown that the presence of uncorrelated structures tends to boost both the SL cross-section for giant arcs and the size of the *Einstein* radii. As discussed, an accurate description of the contribution of uncorrelated large-scale structures needs expensive multiplane ray-tracing simulations and is beyond the purpose of this paper.

However in order to give a hint on how much the *Einstein* radii change including more matter along the line of sight, in Fig. 5 we show the relative size of the *Einstein* radius – with respect to the case in which we select a region of 8 Mpc h^{-1} along the line of sight – computed selecting a region of 16 Mpc h^{-1} (left) and 32 Mpc h^{-1} (right) along the line of sight. From the figure, we can observe that the median value is consistent with unity (filled blue points) and that, in some cases, large-scale structures may boost the size of the *Einstein* radius even by 30 per cent, we notice also that this population is less then 5 per cent of the whole sample. The shaded regions in the figure enclose the first and the third quartiles of the distribution at fixed θ_E. In each panel, the solid line encloses 95 per cent of the data. The histogram in the right subpanels shows the distribution along the y-axis together with the value of the standard deviation of the distributions.

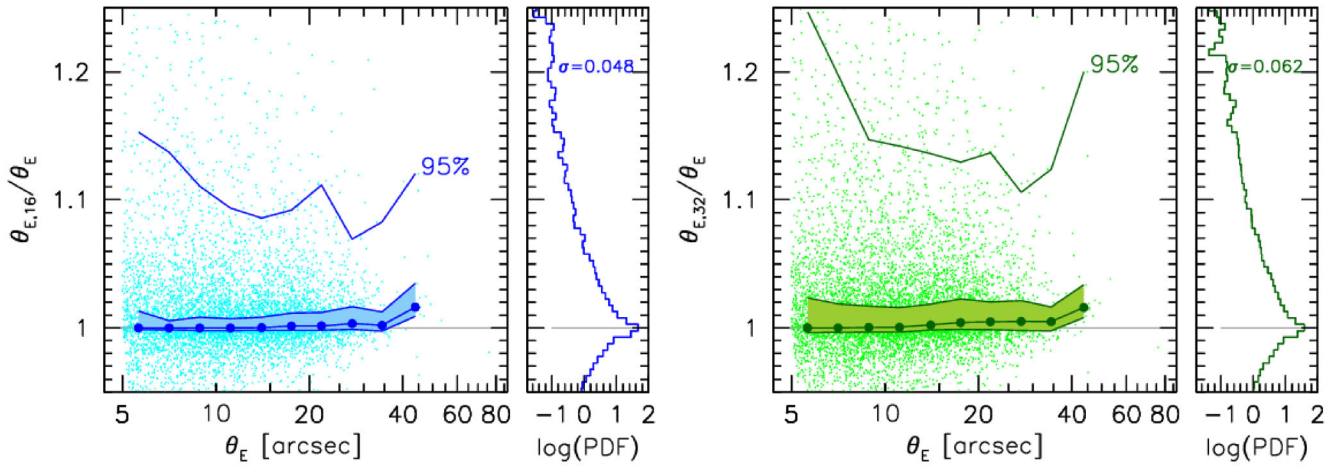

Figure 5. Relative change of the *Einstein* radius of SLCs extracted from the M-XXL simulation when we include all the matter from a region up to 16 Mpc h^{-1} (left) and 32 Mpc h^{-1} along the line of sight. As a reference, we consider the *Einstein* radii as computed from the run where we select all the matter up to 8 Mpc h^{-1}. The filled circle points show the median of the distribution, while the shaded area encloses the first and the third quartiles of the distribution at fixed θ_E.

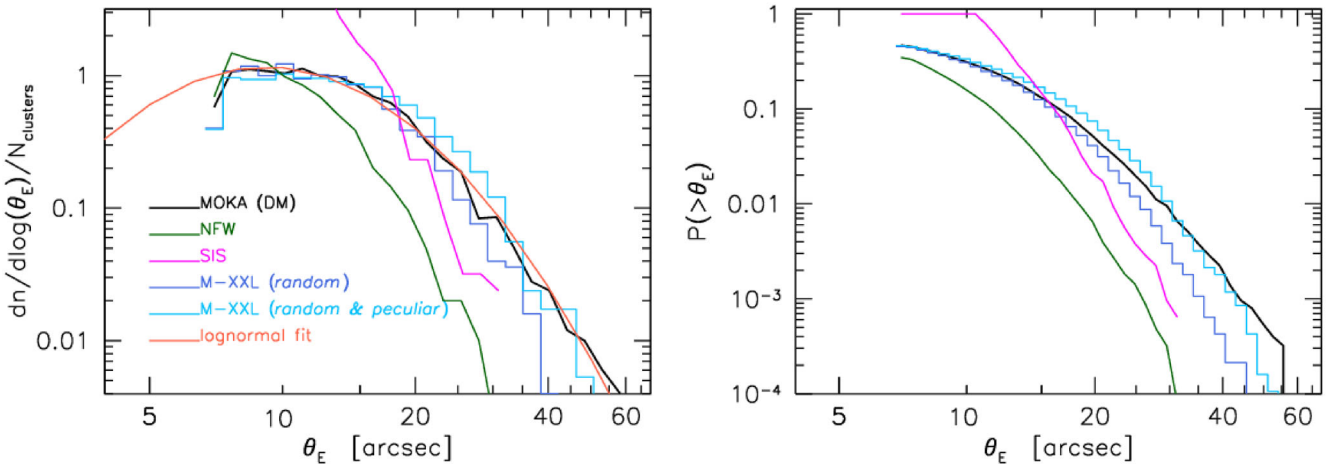

Figure 6. Differential (left-hand panel) and cumulative (right-hand panel) *Einstein* radius distributions in M-XXL and MOKA clusters. The blue and cyan histograms show the distributions measured in the M-XXL simulation considering only the random projections and all the six ones, respectively. The black curve represents the predictions obtained with a MOKA DM run on the same cluster masses, while the green and magenta ones are the predictions for the same masses assuming a smooth NFW or SIS halo profile for the lenses.

2.2 SL models of clusters using the moka code

Running and analysing large numerical simulations are usually non-trivial tasks; in addition, performing self-consistent lensing analysis of different cosmological models including also baryon physics requires large computational resources and various post-processing pipelines. However, the results from different numerical simulations – *N*-body only or including hydrodynamical processes – can be implemented using a pseudo-analytic approach to construct convergence maps of different galaxy clusters in various physical cases as, done with the MOKA code (Giocoli et al. 2012a). MOKA pseudo-analytically reconstructs high-resolution convergence maps of galaxy clusters free from particles and numerical resolution limitations, implementing results obtained from the most recent numerical runs. The virial mass of a halo is defined as

$$M_{\rm vir} = \frac{4\pi}{3} R_{\rm vir}^3 \frac{\Delta_{\rm vir}}{\Omega_{\rm m}(z)} \Omega_0 \rho_{\rm c}, \tag{12}$$

where $\rho_{\rm c}$ represents the critical density of the Universe, $\Omega_0 = \Omega_{\rm m}(0)$ the matter density parameter at the present time and $\Delta_{\rm vir}$ is the virial overdensity (Eke, Cole & Frenk 1996; Bryan & Norman 1998), $R_{\rm vir}$ symbolizes the virial radius of the halo which defines the distance from the halo centre that encloses the desired density contrast. Haloes typically follow the NFW profile and are assumed to be triaxial – following the model by Jing & Suto (2002) and randomly oriented with respect to the line of sight. Each system is also populated by DM substructures assuming the subhalo population model by Giocoli et al. (2010). In modelling the subhalo density profiles, we account for tidal stripping due to close interactions with the main halo smooth component and to close encounters with other clumps, gravitational heating, and dynamical friction (Hayashi et al. 2003; van den Bosch, Tormen & Giocoli 2005; Choi, Weinberg & Katz 2007; Giocoli, Tormen & van den Bosch 2008) using a truncated singular isothermal sphere (SIS; Metcalf & Madau 2001). For the halo concentration–mass relation, we use the Zhao et al. (2009) model which links the concentration of a given halo with the time ($t_{0.04}$) at which its main progenitor assembles 4 per cent of its mass – each halo mass accretion history is computed using the results by Giocoli et al. (2012b). Haloes may also be populated by galaxies according to an HOD approach (Wang et al. 2006) and once settled the central galaxy, with a given stellar mass profile, the surrounding DM distribution can adiabatically contract (Blumenthal et al. 1986; Keeton 2001; Gnedin et al. 2011). To model the stellar mass density profile, MOKA has two implementations: the Hernquist (Hernquist 1990) and Jaffe (Jaffe 1983) profiles. Both for the Hernquist and the Jaffe profiles, we compute the central galaxy scale radius $r_{\rm g}$ from the half-mass (or effective) radius $R_{\rm e}$ by $r_{\rm g} = 0.551 R_{\rm e}$ and as done by Keeton (2001) we define the effective radius to be $R_{\rm e} = 0.003 R_{\rm vir}$. The contribution of all the components are then summed together to compute the cluster convergence map as it can be read from the relation:

$$\kappa(x, y) = \kappa_{\rm DM}(x, y) + \kappa_{\rm star}(x, y) + \sum_{i=1}^{N} \kappa_{{\rm sub},i}(x - x_{{\rm c},i}, y - y_{{\rm c},i}), \tag{13}$$

where $x_{{\rm c},i}$ and $y_{{\rm c},i}$ represent the coordinates of the centre of mass of the ith substructure. The code is very fast and allows not only to study the dependence of lensing observables on the halo properties but also to perform different cosmological studies (Boldrin et al. 2012, 2016) and comparisons with various observational data (Xu et al. 2016), presenting great complementarity also with approaches used in various observational studies (Jullo et al. 2007; More et al. 2012).

In Fig. 6, we compare the *Einstein* radius distributions of different MOKA cluster realizations of the mass sample extracted from the M-XXL catalogue at $z = 1$ having $M_{200} > 3 \times 10^{14}\,{\rm M}_\odot\,h^{-1}$ and $\theta_{\rm E} > 7$ arcsec. We remind the reader that for this comparison we did not generate haloes from the corresponding theoretical mass function but we provide MOKA a sample of clusters with the same masses as the ones in the M-XXL simulation extracted at $z = 1$. Lenses are then located at $z_{\rm l} = 0.5$ and sources at $z_{\rm s} = 2.5$. On the left, we show the differential distributions normalized to the total number of clusters while on the right the cumulative ones. To be consistent with the numerical simulation, MOKA haloes have been generated without a Brightest Central Galaxy (BCG) and have a concentration–mass relation as for the M-XXL cosmology at $z = 1$, computed using the Zhao et al. (2009) model adopting the Giocoli et al. (2012b) halo mass accretion history model. The blue and the cyan histograms show the measurements from the M-XXL considering only the three *random projections* and considering all the six

Table 2. Summary of MOKA runs performed with different models for the central galaxy.

Run	Triaxiality	Minimum m_{sb}	BCG profile	DM adiabatic contraction
sDM	NO	$10^{10}\,M_\odot\,h^{-1}$&$10^{12}\,M_\odot\,h^{-1}$	NO	NO
DM	YES	$10^{10}\,M_\odot\,h^{-1}$	NO	NO
H	YES	$10^{10}\,M_\odot\,h^{-1}$	Hernquist	YES
J	YES	$10^{10}\,M_\odot\,h^{-1}$	Jaffe	YES

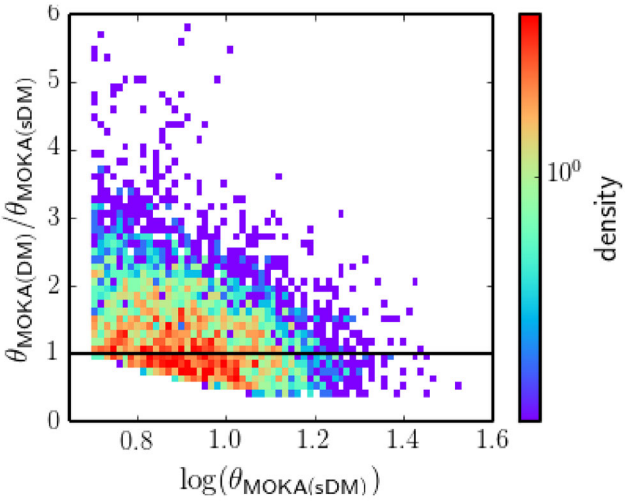

Figure 7. Effect of triaxiality in distorting the size of the *Einstein* radius. Relative size of the *Einstein* radius between a smooth spherical and triaxial NFW halo as obtained from MOKA.

ones – *random* plus *peculiar projections*, respectively. The MOKA maps have been created with a resolution of 1024 × 1024 pixels and are extended up to the virial radius scale of the cluster. As in the M-XXL analysis, we compute the lensing potential and the shear going in the Fourier space and to avoid artificial boundary effects we enclose the maps in a zero-padded region of 512 pixels. The black solid line shows the predictions for different MOKA realizations of the same cluster mass sample. For comparison, the green and the magenta curves show the *Einstein* radius distributions computed assuming a smooth spherical NFW (Navarro, Frenk & White 1996) and SIS halo sample. The latter profile is typically used to predict the location of SL images in elliptical galaxies (Koopmans et al. 2006, 2009). We estimate the velocity dispersion of the SIS halo, we adopt the definition depending on the halo virial mass and radius according to the spherical collapse model (Wu, Fang & Xu 1998; Cooray & Sheth 2002). The figure suggests a quite good consistence in the *Einstein* radius statistics between MOKA and M-XXL clusters, and also that a simple spherical NFW model highly underpredicts the SL capability of SLCs with respect to a triaxial and substructured case. As done by Zitrin et al. (2012), we describe our results with a lognormal distribution (red curve in the left-hand panel of the figure): the relation has $\mu = 2.219$ and $\sigma = 0.532$ normalized consistently as done for the computed distribution from our data; approximately 47 per cent of the clusters with $M_{200} > 3 \times 10^{14}\,M_\odot\,h^{-1}$ possess an *Einstein* radius larger than 7 arcsec.

In Figs 7 and 8, we discuss the effect of triaxiality and substructures on the size of the *Einstein* radius. Going step-by-step, in the first figure we compare the size of the *Einstein* radii of the same sample of haloes when running MOKA with the triaxiality off (spherical sDM) and on (triaxial DM), keeping identical all the other cluster and map properties. The effect of triaxiality, as already discussed by different authors studying haloes in numerical simulations (Jing & Suto 2002; Despali, Giocoli & Tormen 2014), is quite crucial and typically tends to boost the *Einstein* radius even by a factor of 4. Nevertheless, it is important to observe that the scatter around unity is quite asymmetric and depends on how the halo ellipsoid – typically prolate – is oriented with respect to the line of sight. On the other side, in Fig. 8 we isolate the effect of substructures performing two sets of simulations for our halo sample. In the first, we consider a spherical DM halo populated with substructures down to $m_{sb} = 10^{10}\,M_\odot\,h^{-1}$ and in the second down to $10^{12}\,M_\odot\,h^{-1}$ for the minimum subhalo mass and compare their results with respect to a smooth and spherical NFW sample. In the left-hand panel of the figure, we compare the size of *Einstein* radii of clusters in our first run with respect to the size computed from a smooth NFW halo with the same mass and concentration. We remind the reader that in populating a halo with substructures we use the model by Giocoli et al. (2010) for the subhalo mass function and the results by Gao et al. (2004) for the subhalo distribution in the host. Once the subhalo mass function is sampled, we compute the total mass in subhaloes and subtract it to the input halo mass to compute the smooth halo component, to which we assign a concentration such that the mass density profile of the smooth plus clump components matches the input assigned concentration. In the right-hand panel of Fig. 8, we show the probability distribution function of the relative *Einstein* radius variation between the smooth NFW halo and the substructured runs with the two different minimum subhalo mass thresholds. We notice that the presence of small substructures tends to perturb the size of the *Einstein* radius, but are the most massive ones that mainly contribute to distort the SL regions – although this depends on the relative distance of the perturber from the critical curves of the cluster.

A correct treatment of the mass density distribution in the central region of the cluster is very important for SL modellings and predictions (Meneghetti, Bartelmann & Moscardini 2003). Numerical simulations and semi-analytical models forecast that merger events (Springel et al. 2001; De Lucia et al. 2004; Tormen et al. 2004) that drive the formation of DM haloes along the cosmic time bring to the formation of a massive and bright galaxy at the centre of galaxy clusters (Merritt 1985). These central galaxies are typically the brightest galaxies in clusters and are usually referred as BCG. They are the most massive galaxies in the Universe and generally are giant ellipticals: their position correspond approximately to the geometric and kinematic centre of the cluster and to the position of the peak of the X-ray emission. Nevertheless, it is interesting to mention that there are clusters where these conditions are not all satisfied at the same time: typically this happens in systems that are not completely relaxed and present merging events (Katayama et al. 2003; Sanderson, Edge & Smith 2009; Zhang et al. 2016). For the density distribution of the stars in the BCG, in our analyses we make use of two different parametrizations: the Hernquist (Hernquist 1990) and the Jaffe (Jaffe 1983) profiles. We remind the reader that in running MOKA with these parametrizations we (i) assign the stellar mass to the BCG using an HOD formalism

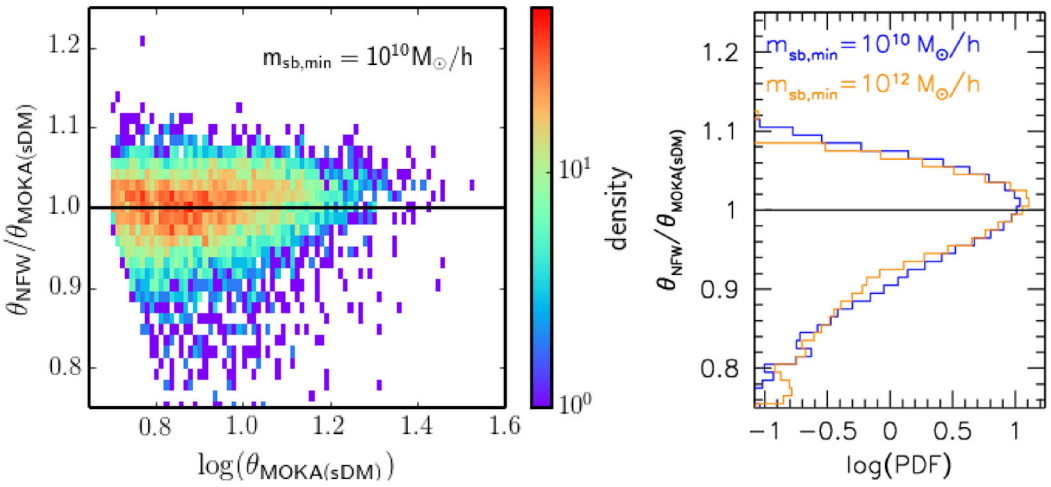

Figure 8. Effect of substructures in perturbing the *Einstein* radius of galaxy clusters. Relative variation of the size of the *Einstein* radius in presence of substructures. To isolate the effect, we consider the case of spherical clusters. In the left-hand panel, we show the density probability distribution of the relative variation assuming $10^{10}\,M_\odot\,h^{-1}$ as minimum subhalo mass. In the right-hand panel, we present the probability distribution function distributions of the *Einstein* radius variation for the two subhalo minimum mass cases: 10^{10} and $10^{12}\,M_\odot\,h^{-1}$.

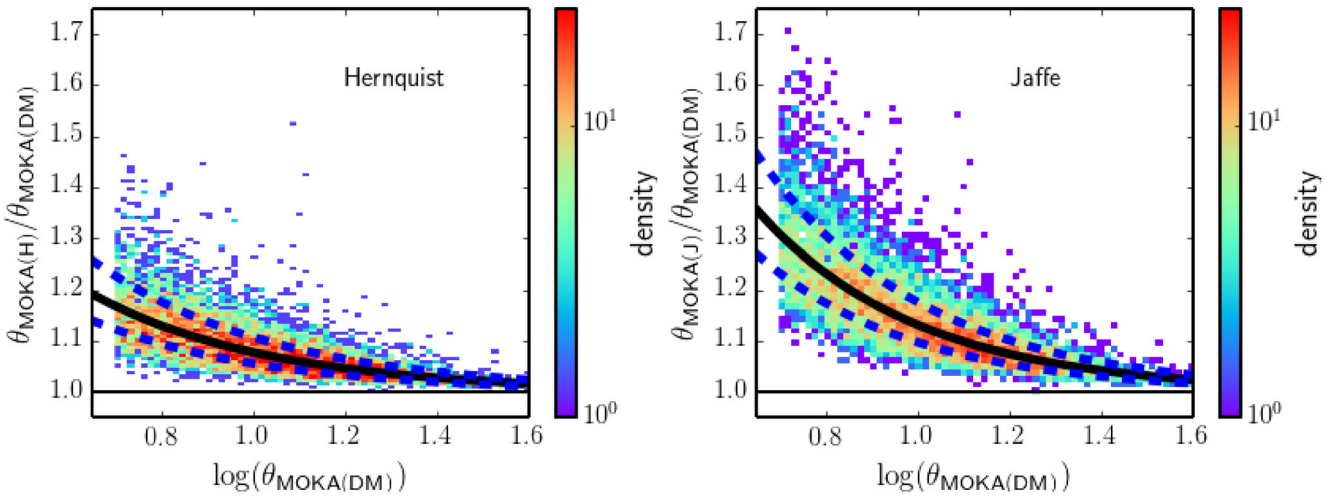

Figure 9. Influence of the presence of a BCG in modifying the size of the *Einstein* radius. Left- and right-hand panels refer to the case of a BCG with a Hernquist and Jaffe profile, respectively. The solid curve in each panel represents the best-fitting relation to the scatter distribution as it can be read from equation (14). The dashed curve shows 1σ uncertainties on the measured best-fitting parameters.

(Wang et al. 2006), (ii) conserve the total mass in the cluster and (iii) allow the DM density distribution to adiabatically contract (Keeton 2003; Giocoli et al. 2012a).

In Fig. 9, we show the relative size of the *Einstein* radius for SLCs (with $\theta_E > 5$ arcsec – below which our measurements may be affected by the grid size of the map) between a pure DM run and a set of simulations that assume a Hernquist (left-hand panel) and a Jaffe profile (right-hand panel) for the BCG. Because of the different behaviour of the profile, the two models give quite different relative results. We remind the reader that while the Hernquist profile has a logarithmic slope in the inner part of -1, the Jaffe profile goes like -2 and both profiles in the outskirts of the BCG proceed like -4. From the figure, we notice that for smaller values of *Einstein* radii the results are dominated by the mass density distribution of the BCG, on the contrary for larger values of θ_E they are influenced by the DM profile: triaxiality plus clumpiness of the halo. In the figures, the solid curves represent the best-fitting relation to the scattered data points; they can be, respectively, read as

$$\theta_E/\theta_{E,(DM)} = \mathbf{A}\,\exp\left(\beta\theta_{E,(DM)}\right)$$
$$\text{Hernquist}\quad \mathbf{A} = 0.024^{+0.251}_{-0.281}\quad \beta = -2.579^{+0.070}_{-0.051}$$
$$\text{Jaffe}\quad \mathbf{A} = 0.817^{+0.217}_{-0.242}\quad \beta = -2.843^{+0.075}_{-0.059}; \qquad (14)$$

the dashed curves show the 1σ uncertainties on the relations.

The benefit of having these fitting functions is illustrated in Fig. 10, where we compare the cumulative probability distribution computed from a pure DM run (black curve) and from the two runs that assume the Hernquist (orange curve) and Jaffe (purple curve) profiles for the central galaxy. In the bottom panel, we present the relative residuals of the cumulative distributions of the two runs with BCG with respect to the DM-only case. The presence of a BCG increases the probability of having a cluster with an *Einstein* radius larger than $\theta_E > 10$ arcsec of about 10–20 per cent

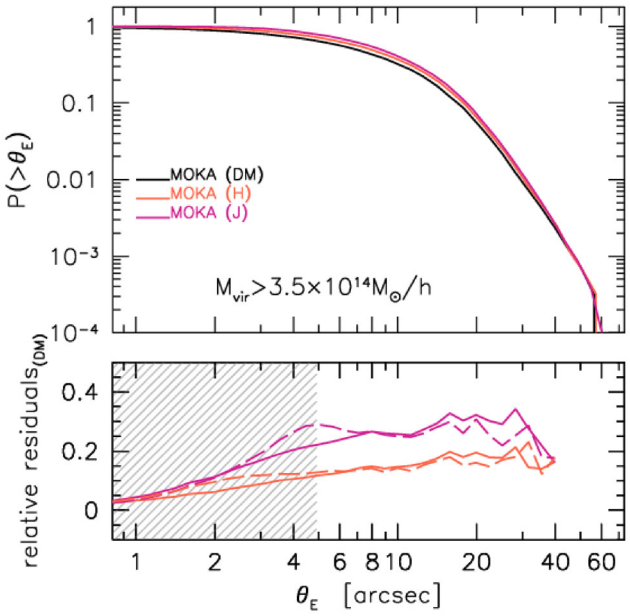

Figure 10. Cumulative probability distribution of having a cluster with an *Einstein* radius larger than a given value. Black, orange and salmon coloured curves show the distribution computed from a MOKA Monte Carlo Simulation of the M-XXL mass sample assuming no BCG (DM) a BCG with a Hernquist (H) or a Jaffe (J) profile, respectively. The solid curves in the bottom panel show the relative residuals of the distributions with respect to the DM only case. The dashed curves refer to the predictions of the *Einstein* radius distributions computed for the two cases from the DM run using the relation as in equation (14).

– depending on the density profile model of the central galaxy. In the bottom panel, the two corresponding dashed coloured curves show the relative distributions obtained from the pure DM results and accounting for the BCG contribution sampling the best-fitting relations as in equation (14) with their appropriate scatter for the parameters.

3 SL SCALING RELATIONS

In this section, we discuss the correlation of the size of the *Einstein* radius with other galaxy cluster properties. In the figures, we will present we have used the only-DM MOKA runs; the relations obtained considering runs with a BCG following a Hernquist and a Jaffe profile will be summarized in Table 3.

The first correlation we have considered is between the cluster mass and the size of the *Einstein* radius (see Fig 11). In this case, as it is evident from the figure, the two quantities do not show a good correlation: we argue that this is probably due to the fact that what mainly matters in shaping the *Einstein* radius is the halo triaxiality, the concentration and the presence of substructures; but we are observing in the plane of the sky a random orientation of the cluster. The second attempt has been done by correlating the weak lensing mass of the clusters with the *Einstein* radii. Using a Navarro–Frank–White (NFW; Navarro et al. 1996; Navarro, Frenk & White 1997) model for the matter density profile, it is possible to compute the associated shear profile $\gamma_{\rm NFW}$ once the lens and the source redshifts have been fixed. For each simulated convergence map, we compute the spherical average shear profile and

Table 3. Best-fitting linear coefficients – $y = mx + q$ – of all the runs (DM, Hernquist and Jaffe) of the relation displayed in Figs 12 and 13. The superscript and underscript numbers present the coefficient of the least squares in the $x - y$ and $y - x$ planes, respectively.

Run	m	q
	$\log(M_{\rm wl}) - \log(\theta_{\rm E})$	
DM	$0.899^{0.615}_{1.293}$	$13.672^{13.957}_{13.275}$
Hernquist	$0.892^{0.652}_{1.206}$	$13.641^{13.884}_{13.322}$
Jaffe	$0.894^{0.694}_{1.143}$	$13.589^{13.791}_{13.336}$
	$\log(\theta_{\rm E}(M_{\rm wl}, c_{\rm wl})) - \log(\theta_{\rm E})$	
DM	$1.121^{1.030}_{1.221}$	$-0.188^{-0.091}_{-0.295}$
Hernquist	$1.153^{1.066}_{1.249}$	$-0.226^{-0.132}_{-0.330}$
Jaffe	$1.168^{1.089}_{1.254}$	$-0.238^{-0.153}_{-0.331}$

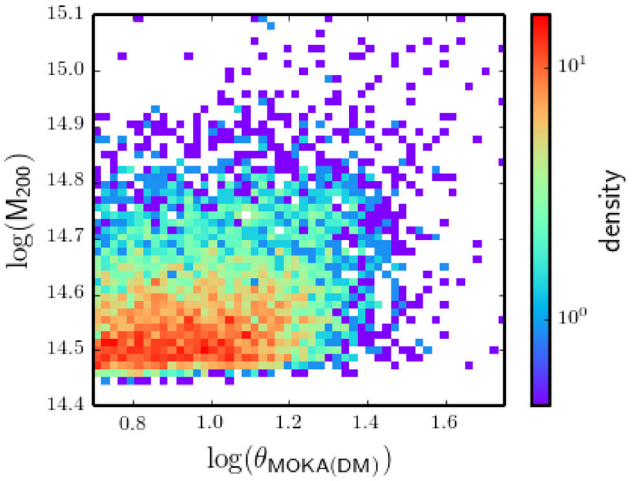

Figure 11. Correlation between the cluster masses and the measured size of the *Einstein* radii from the two-dimensional convergence maps. The colours show the point density of clusters of the DM-only MOKA run in the log (M_{200})–log $(\theta_{\rm E})$ space.

measure the associated weak lensing mass $M_{\rm wl}$ and concentration $c_{\rm wl}$ by minimizing

$$\chi^2(M_{\rm wl}, c_{\rm wl}) = \frac{\sum_i [\gamma(r_i) - \gamma_{\rm NFW}(M_{\rm wl}, c_{wl})]^2}{\sigma^2_{g,i}}; \quad (15)$$

$\sigma_{g,i}$ represents the shape measurement error computed assuming a number density of sources of 20/arcmin^2 – mimicking the number of background sources expected to be usable for weak lensing measurements in future space-based observations:

$$\sigma_{g,i} = \frac{\sigma_\epsilon}{\sqrt{n_g A_i}} \quad (16)$$

being A_i the area of the i-annulus. This method gives typically a good determination of the projected mass responsible for the lensing signal (Hoekstra et al. 2012; Giocoli et al. 2014; von der Linden et al. 2014). To summarize for each cluster – and for each of the corresponding run (DM, Hernquist and Jaffe) – we have measured of the associated weak lensing mass and concentration in addition to the evaluation of the size of the *Einstein* radius. In Fig. 12, we present the scaling relation – in logarithmic space and for the DM-only run – between the weak lensing cluster mass M_{wl} and the corresponding size of the *Einstein* radius. The blue dashed lines show the

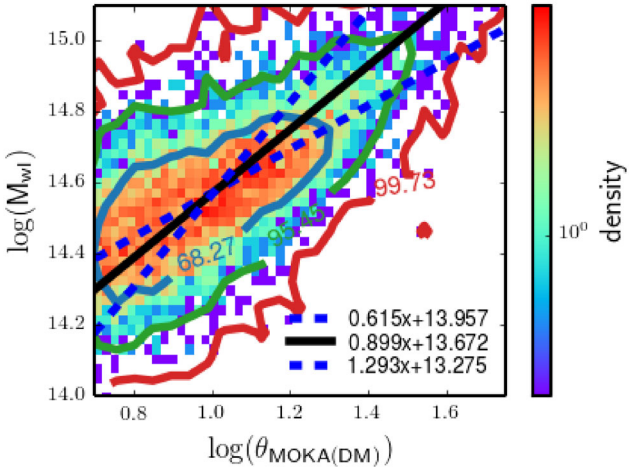

Figure 12. Scaling relation between the weak lensing estimated mass M_{wl} – computing the best fit profile with a NFW functional to the weak lensing shear profile – and the size of the *Einstein* radius. In the figure we show the relation for the DM-only run; results of the other runs are summarized in Table 3. The blue dashed lines show the best least-squares fit to the data points in the $\log(M_{wl}) - \log(\theta_E)$ and in the $\log(\theta_E) - \log(M_{wl})$ spaces, while the black line represents the bisector of them. The blue, green and red contours enclose 68.27, 95.45 and 99.73 per cent of the data points, respectively.

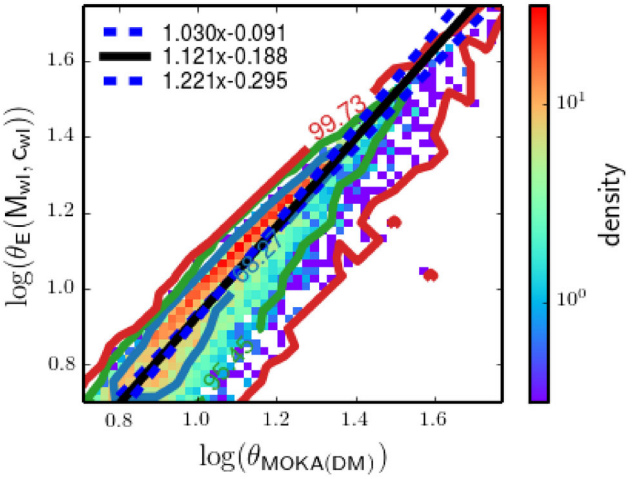

Figure 13. Scaling relation between the *Einstein* radius of an NFW halo with the same mass and concentration – computed by fitting with an NFW functional the weak lensing shear profile – and the size of the *Einstein* radius of the cluster. As in Fig. 12, we show the correlation only for the DM run and present in Table 3 the results for the runs with BCGs. Dashed blue lines show the least-squares fit to the data in the $\log(\theta_E(M_{wl}, c_{wl})) - \log(\theta_E)$ and in the $\log(\theta_E)$–$\log(\theta_E(M_{wl}, c_{wl}))$ spaces, while the black line displays the bisector of them.

least-squares fits in the $\log(M_{wl}) - \log(\theta_E)$ and in the $\log(\theta_E) - \log(M_{wl})$ spaces, while the black line indicates the corresponding bisector of them. The blue, green and red curves enclose 68.27, 95.45 and 99.73 per cent of the data points, respectively. The third relation – which offers a very strict correspondence – we have considered is between the size of the *Einstein* radius associated with an NFW-halo having M_{wl} and c_{wl} and the one we measure from our maps. For an NFW halo, we compute $\theta_E(M, c)$ – given its mass and concentration in addition to the lens and source redshifts – from the profile of $[1 - \kappa(\theta) - \gamma(\theta)]$ and measuring the angular scale where the relation $1 - \kappa(\theta_E) - \gamma(\theta_E) = 0$ holds. In Fig. 13, we display this correlation – again in $\log_{10}$ space for the DM-only run: the results for the runs with BCGs are reported in Table 3. As in the previous figure, the coloured contours enclose enclose 68.27, 95.45 and 99.73 per cent of the data points, the dashed blue lines displays least-squares fit in the $\log(\theta_E(M_{wl}, c_{wl}))$–$\log(\theta_E)$ and in the $\log(\theta_E)$–$\log(\theta_E(M_{wl}, c_{wl}))$ spaces, while the black line their bisector. In this case, we notice that the correlation between the two quantities is very close, apart for some asymmetries – some systems possess an *Einstein* radius larger than the one computed from M_{wl} and c_{wl}. A case by case analysis of these systems has brought to two main causes: (i) large value of the ellipticity in the plane of the sky and (ii) projection of substructures close to the centre of the cluster. Both these give at the end a poor NFW fit to the shear profile, leading to an underestimation of the corresponding *Einstein* radius associated with the NFW profile. We found that the first cause is the most probable in the majority of the cases.

4 SENSITIVITY OF THE *Einstein* RADIUS DISTRIBUTION ON Ω_M AND σ_8

The number density and the properties of galaxy clusters has been investigated by different authors with the aim of understanding how sensible they are to cosmological parameters (Rozo et al. 2010; Waizmann et al. 2012, 2014; Sartoris et al. 2015; Boldrin et al. 2016). In this section, we discuss how the *Einstein* radius distributions are sensitive to the total matter density in the Universe Ω_M – assuming always to live in a flat universe: $\Omega_M + \Omega_\Lambda = 1$ – and to the linear mass density rms on a scale of 8 Mpc h^{-1} σ_8 – that defines the initial matter power spectrum normalization. We always consider lenses located at $z_l = 0.5$ and to obtain their abundance we randomly sample the Sheth & Tormen (1999) mass function between $z = 0.48$ and 0.52. In Fig. 14, we show the probability distribution function (left-hand panels) and cumulative number density per square degrees (right-hand panels) of the *Einstein* radii in cosmological model with different Ω_M (top panels) and σ_8 (bottom panels) parameters – fixing one at a time. The vertical arrows – coloured according to the corresponding cosmological model – indicate the largest *Einstein* radius found in the two extreme samples assuming a full sky realization. From the figure, we notice that the *Einstein* radii regularly increase with Ω_M and σ_8; this is because galaxy clusters are more numerous in these cosmologies but also because they are also more concentrated; in addition, we remind that clusters at $z_l = 0.5$ in universes with higher matter content possess also a lower lensing distance D_{lens}. We underline that the BCG treatment is absent in these simulations and remind the reader that the counts can be adapted to the two considered BCG stellar density profiles at the light of the results discussed in Figs 9 and 10. In the left-hand panels, the black solid curves display the lognormal best relation to the Planck13 counts that can be read as

$$\mathrm{PDF}(\theta_E) = \frac{1}{\sqrt{2\pi\sigma^2}} \exp\left[-\frac{(\ln(\theta_E) - \mu)^2}{2\sigma^2}\right], \quad (17)$$

with $\mu = 1.016$ and $\sigma = 0.754$. From the right-hand panels of the figure, we notice that a change of Ω_M – or σ_8 – of 10 per cent corresponds approximately to a variation in the number of lenses with $\theta_E > 5$ arcsec of about 20 per cent.

In Fig. 15, we display the relative counts of clusters with θ_E larger than 5 arcsec, with respect to the number computed for a Planck13 cosmology, in the Ω_M–σ_8 plane. As reference the black and the blue circles indicate the predicted numbers of these SLCs in the

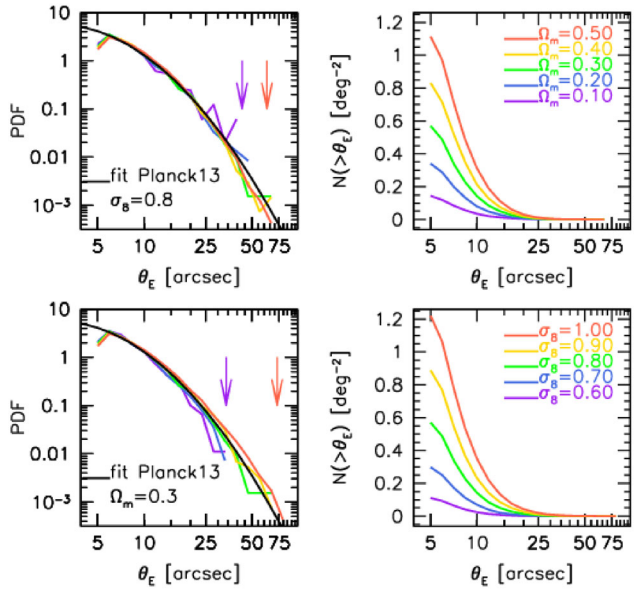

Figure 14. Left-hand panels: probability distribution functions of the *Einstein* radius distributions of a Monte Carlo realization of lenses at redshift $z_l = 0.5$ with sources located at $z_s = 2.5$ – the cluster number density has been computed from the Sheth & Tormen (1999) mass function integrated on the whole sky between $z = 0.48$ and 0.52. Right-hand panels: cumulative number counts of strong lenses per square degrees with an *Einstein* radius larger than a fixed value. Top and bottom panels display the case of varying Ω_M and σ_8 at a time, respectively. The black curve in the left-hand panels represents the lognormal relation (equation 17) that better describes the Planck13 probability distribution function. The arrows on the left-hand panels mark the largest *Einstein* radius find in the two extreme corresponding models.

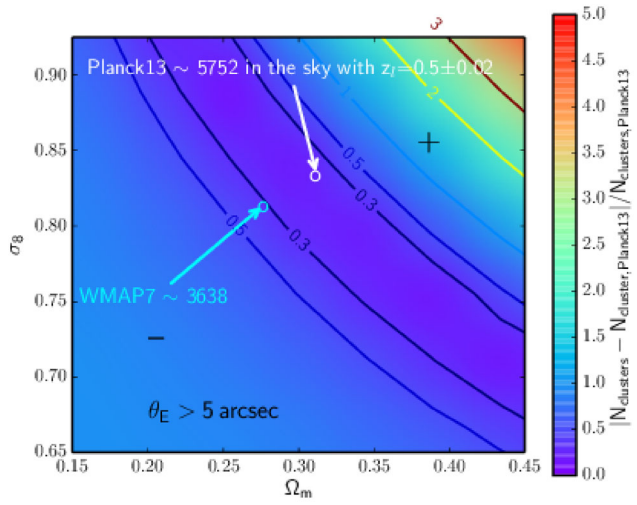

Figure 15. Relative counts of clusters with *Einstein* radius larger than 5 arcsec, with respect to the Planck13 counts, in the Ω_M–σ_8 plane. The black and the blue circles indicate the counts on the full sky for a Planck13 and *WMAP*7 cosmology, respectively. We consider the number density of cluster lenses between $z = 0.48$ and 0.52, with sources at $z_s = 2.5$. A plus and minus signs in the plane indicate the regions where counts are positive and negative with respect to the Planck13 cosmology, respectively.

whole sky between $z_l = 0.48$ and 0.52 for the Planck13 (black circle) and *WMAP*7 (blue cross) cosmologies. For the *WMAP*7 model, we assume $\Omega_M = 0.272$, $\Omega_\Lambda = 0.728$, $h = 0.704$ and $\sigma_8 = 0.809$. These results show that the expected counts of the *Einstein* radii in these two models may differ by more than 3σ assuming a Poisson distribution: 5752 for the Planck13 and 3638 for the *WMAP*7 cosmology, respectively. We remind the reader that in computing the cluster counts for the various cosmological models, we have accounted for the change of volume between $z = 0.48$ and 0.52. In particular, the *WMAP*7 model has a volume (in (Mpc h^{-1})^3) of about 5 per cent larger than the Planck13 one because of a higher Hubble constant and lower total matter content, but fewer SLC counts. This highlights that the change of volume is quite negligible with respect to the role played by the initial power spectrum normalization parameter σ_8 and by the different total matter content Ω_M for the SLC counts: in Planck13, we find more clusters and those are more concentrated than in the *WMAP*7 cosmology because formed at higher redshifts. As already noticed by Boldrin et al. (2016), the degeneracy relation of the SLC counts behaves as the cluster counts plus the evolution of the halo structural properties in different cosmological models and the variation of the lensing distance.

5 SUMMARY AND CONCLUSIONS

In this paper, we have presented the SL properties of a sample of galaxy clusters extracted from the M-XXL simulation analysing the distribution of their *Einstein* radius. The results have been compared with a Monte Carlo MOKA realization of the same mass sample finding very good agreement. We have also performed an analysis to understand how sensitive is the *Einstein* radius distribution on specific cosmological parameters creating a sample of clusters in different models using the MOKA code. We find that the *Einstein* radius distribution is quite sensitive to Ω_M and σ_8, as it is the cluster abundance, and that universes with high values of Ω_M and σ_8 possess a large number of SLCs.

In the following points, we summarize the main results of our analyses:

(i) a large fraction of SLCs are systematically biased by projection effects;

(ii) the orientation matters: when the major axis of the cluster ellipsoid is oriented along the line of sight, the *Einstein* radius may be boosted by more then a factor of 2 with respect to a random orientation;

(iii) the shape of the SL population is slightly more triaxial than the overall considered cluster sample;

(iv) a self-consistent treatment of the effects of large-scale structures is important for SL predictions: correlated systems may boost the *Einstein* radius of galaxy clusters by even more than 30 per cent;

(v) the comparison between M-XXL clusters and MOKA realizations on the same sample of cluster masses shows consistent results for the *Einstein* radius distribution, and is well described by a lognormal distribution;

(vi) a correct treatment of the subhalo population and the cluster triaxiality is important for an adequate SL modelling: typically, the triaxiality matters more and may boost the size of the cluster *Einstein* radii by various orders of magnitudes;

(vii) the presence of a BCG in a cluster tends to modify the total projected mass profile and consistently the size of the *Einstein* radius; we have discussed and modelled the impact of two different stellar mass density profiles (Jaffe 1983; Hernquist 1990) on the SL properties and noticed that the *Einstein* radii may change by

10–60 per cent – depending on the cluster properties and stellar profiles;

(viii) the size of the *Einstein* radius has a quite tight correlation with the *Einstein* radius of a NFW halo where mass and concentration are computed performing a fit to the weak lensing shear profile; less stringent is the correlation with the weak lensing mass;

(ix) the *Einstein* radius distribution is very sensitive to the matter content of the Universe (Ω_M) and to the initial power spectrum normalization (σ_8): we have noticed that universes with larger values of those parameters possess a higher number of SLCs; this can help distinguish Planck13 and *WMAP*7 cosmology at 3σ.

In conclusion, our results encourage in shading more light into the dark components of our Universe through the study of SLC populations, foreseeing the unique results that will be available from the next-generation wide field surveys from space.

ACKNOWLEDGEMENTS

CG thanks CNES for financial support. ML acknowledges the Centre National de la Recherche Scientifique (CNRS) for its support. This work was performed using facilities offered by CeSAM (Centre de donneS Astrophysique de Marseille- http://lam.oamp.fr/cesam/). This work was granted access to the HPC resources of Aix-Marseille Universite financed by the project Equip@Meso (ANR-10-EQPX-29-01) of the programme 'Investissements d'Avenir' supervised by the Agence Nationale pour la Recherche (ANR). This work was carried out with support of the OCEVU Labex (ANR- 11-LABX-0060) and the A*MIDEX project (ANR-11-IDEX- 0001-02) funded by the 'Investissements d'Avenir' French government programme managed by the ANR. We acknowledge support from the Programme National de Cosmologie et Galaxie (PNCG). MM acknowledges support from Ministry of Foreign Affairs and International Cooperation, Directorate General for Country Promotion, from INAF via PRIN-INAF 2014 1.05.01.94.02, and from ASI via contract ASI/INAF/I/023/12/0. LM acknowledges the grants ASI n.I/023/12/0 'Attività relative alla fase B2/C per la missione *Euclid*', MIUR PRIN 2010-2011 'The dark Universe and the cosmic evolution of baryons: from current surveys to *Euclid*' and PRIN INAF 2012 'The Universe in the box: multiscale simulations of cosmic structure'. REA acknowledges support from AYA2015-66211-C2-2. EJ acknowledge CNES support. CG thanks Mauro Sereno, Jesus Vega and Michele Boldrin for useful discussions and PYTHON stratagems. We also thank Giuseppe Tormen and Vincenzo Mezzalira for giving us the possibility to use their computer facilities on which part of the MOKA simulations have been run.

REFERENCES

Angulo R. E., Springel V., White S. D. M., Jenkins A., Baugh C. M., Frenk C. S., 2012, MNRAS, 426, 2046
Angulo R. E., Chen R., Hilbert S., Abel T., 2014, MNRAS, 444, 2925
Atek H. et al., 2014, ApJ, 786, 60
Bacon D. J., Amara A., Read J. I., 2010, MNRAS, 409, 389
Bartelmann M., 2010, Class. Quantum Grav., 27, 233001
Bartelmann M., Schneider P., 2001, Phys. Rep., 340, 291
Bellagamba F., Maturi M., Hamana T., Meneghetti M., Miyazaki S., Moscardini L., 2011, MNRAS, 413, 1145
Blumenthal G. R., Faber S. M., Flores R., Primack J. R., 1986, ApJ, 301, 27
Boldrin M., Giocoli C., Meneghetti M., Moscardini L., 2012, MNRAS, 427, 3134
Boldrin M., Giocoli C., Meneghetti M., Moscardini L., Tormen G., Biviano A., 2016, MNRAS, 457, 2738
Bonamigo M., Despali G., Limousin M., Angulo R., Giocoli C., Soucail G., 2015, MNRAS, 449, 3171
Borgani S., Kravtsov A., 2011, Adv. Sci. Lett., 4, 204
Boylan-Kolchin M., Springel V., White S. D. M., Jenkins A., Lemson G., 2009, MNRAS, 398, 1150
Bradač M. et al., 2006, ApJ, 652, 937
Broadhurst T., Huang X., Frye B., Ellis R., 2000, ApJ, 534, L15
Bryan G. L., Norman M. L., 1998, ApJ, 495, 80
Choi J.-H., Weinberg M. D., Katz N., 2007, MNRAS, 381, 987
Codis S., Pichon C., Pogosyan D., 2015, MNRAS, 452, 3369
Coe D. et al., 2013, ApJ, 762, 32
Cooray A., Sheth R., 2002, Phys. Rep., 372, 1
De Lucia G., Kauffmann G., Springel V., White S. D. M., Lanzoni B., Stoehr F., Tormen G., Yoshida N., 2004, MNRAS, 348, 333
Despali G., Giocoli C., Tormen G., 2014, MNRAS, 443, 3208
Despali G., Giocoli C., Angulo R. E., Tormen G., Sheth R. K., Baso G., Moscardini L., 2016, MNRAS, 456, 2486
Donahue M. et al., 2016, ApJ, 819, 36
Donnarumma A. et al., 2011, A&A, 528, A73
Einstein A., 1918, Sitz. Königlich Preußischen Akad. Wiss. Seite, Berlin, p. 448
Eke V. R., Cole S., Frenk C. S., 1996, MNRAS, 282, 263
Formicola I., Radovich M., Meneghetti M., Mazzotta P., Grado A., Giocoli C., 2016, MNRAS, 458, 2776
Gao L., White S. D. M., Jenkins A., Stoehr F., Springel V., 2004, MNRAS, 355, 819
Giocoli C., Tormen G., van den Bosch F. C., 2008, MNRAS, 386, 2135
Giocoli C., Tormen G., Sheth R. K., van den Bosch F. C., 2010, MNRAS, 404, 502
Giocoli C., Meneghetti M., Bartelmann M., Moscardini L., Boldrin M., 2012a, MNRAS, 421, 3343
Giocoli C., Tormen G., Sheth R. K., 2012b, MNRAS, 422, 185
Giocoli C., Meneghetti M., Metcalf R. B., Ettori S., Moscardini L., 2014, MNRAS, 440, 1899
Giocoli C. et al., 2016, MNRAS, in press
Gnedin O. Y., Ceverino D., Gnedin N. Y., Klypin A. A., Kravtsov A. V., Levine R., Nagai D., Yepes G., 2011, preprint (arXiv:1108.5736)
Guzzo L. et al., 2014, A&A, 566, A108
Hayashi E., Navarro J. F., Taylor J. E., Stadel J., Quinn T., 2003, ApJ, 584, 541
Hennawi J. F., Dalal N., Bode P., Ostriker J. P., 2007, ApJ, 654, 714
Hernquist L., 1990, ApJ, 356, 359
Hilbert S., White S. D. M., Hartlap J., Schneider P., 2008, MNRAS, 386, 1845
Hoekstra H., Mahdavi A., Babul A., Bildfell C., 2012, MNRAS, 427, 1298
Hoekstra H., Bartelmann M., Dahle H., Israel H., Limousin M., Meneghetti M., 2013, Space Sci. Rev., 177, 75
Jaffe W., 1983, MNRAS, 202, 995
Jing Y. P., Suto Y., 2002, ApJ, 574, 538
Jullo E., Kneib J.-P., Limousin M., Elíasdóttir Á., Marshall P. J., Verdugo T., 2007, New J. Phys., 9, 447
Jullo E., Natarajan P., Kneib J.-P., D'Aloisio A., Limousin M., Richard J., Schimd C., 2010, Science, 329, 924
Katayama H., Hayashida K., Takahara F., Fujita Y., 2003, ApJ, 585, 687
Keeton C. R., 2001, ApJ, 561, 46
Keeton C. R., 2003, ApJ, 584, 664
Koopmans L. V. E., Treu T., Bolton A. S., Burles S., Moustakas L. A., 2006, ApJ, 649, 599
Koopmans L. V. E. et al., 2009, ApJ, 703, L51
Landau L. D., Lifshitz E. M., 1971, The Classical Theory of Fields. Pergamon Press, Oxford
Laureijs R. et al., 2011, preprint (arXiv:1110.3193)
Le Fèvre O. et al., 2015, A&A, 576, A79
Limousin M. et al., 2016, A&A, 588, A99
Lynds R., Petrosian V., 1986, BAAS, 18, 1014
Macciò A. V., Dutton A. A., van den Bosch F. C., 2008, MNRAS, 391, 1940
Meneghetti M., Bartelmann M., Moscardini L., 2003, MNRAS, 346, 67
Meneghetti M. et al., 2008, A&A, 482, 403

Meneghetti M., Rasia E., Merten J., Bellagamba F., Ettori S., Mazzotta P., Dolag K., Marri S., 2010a, A&A, 514, A93
Meneghetti M., Fedeli C., Pace F., Gottlöber S., Yepes G., 2010b, A&A, 519, A90
Meneghetti M., Fedeli C., Zitrin A., Bartelmann M., Broadhurst T., Gottlöber S., Moscardini L., Yepes G., 2011, A&A, 530, A17
Merritt D., 1985, ApJ, 289, 18
Merten J., 2014, preprint (arXiv:1412.5186)
Merten J. et al., 2015, ApJ, 806, 4
Metcalf R. B., Madau P., 2001, MNRAS, 563, 9
More A., Cabanac R., More S., Alard C., Limousin M., Kneib J.-P., Gavazzi R., Motta V., 2012, ApJ, 749, 38
Navarro J. F., Frenk C. S., White S. D. M., 1996, ApJ, 462, 563
Navarro J. F., Frenk C. S., White S. D. M., 1997, ApJ, 490, 493
Newman A. B., Treu T., Ellis R. S., Sand D. J., 2011, ApJ, 728, L39
Oguri M., Blandford R. D., 2009, MNRAS, 392, 930
Oguri M., Takada M., Umetsu K., Broadhurst T., 2005, ApJ, 632, 841
Paczynski B., 1987, Nature, 325, 572
Percival W. J. et al., 2014, MNRAS, 439, 2531
Petkova M., Metcalf R. B., Giocoli C., 2014, MNRAS, 445, 1954
Planck Collaboration I, 2014, A&A, 571, A1
Postman M. et al., 2012, ApJS, 199, 25
Puchwein E., Hilbert S., 2009, MNRAS, 398, 1298
Radovich M. et al., 2015, A&A, 579, A7
Rau S., Vegetti S., White S. D. M., 2013, MNRAS, 430, 2232
Redlich M., Bartelmann M., Waizmann J.-C., Fedeli C., 2012, A&A, 547, A66
Richard J., Pelló R., Schaerer D., Le Borgne J.-F., Kneib J.-P., 2006, A&A, 456, 861
Rozo E. et al., 2010, ApJ, 708, 645
Saha P., Williams L. L. R., 2006, ApJ, 653, 936
Sand D. J., Treu T., Ellis R. S., 2002, ApJ, 574, L129
Sanderson A. J. R., Edge A. C., Smith G. P., 2009, MNRAS, 398, 1698
Sartoris B. et al., 2015, MNRAS, 459, 1764
Serjeant S., 2014, ApJ, 793, L10
Sharon K., Gladders M. D., Rigby J. R., Wuyts E., Bayliss M. B., Johnson T. L., Florian M. K., Dahle H., 2014, ApJ, 795, 50
Shaw L. D., Weller J., Ostriker J. P., Bode P., 2006, ApJ, 646, 815
Sheth R. K., Tormen G., 1999, MNRAS, 308, 119
Soucail G., Fort B., Mellier Y., Picat J. P., 1987, A&A, 172, L14
Soucail G., Mellier Y., Fort B., Cailloux M., 1988a, A&AS, 73, 471
Soucail G., Mellier Y., Fort B., Mathez G., Cailloux M., 1988b, A&A, 191, L19
Soucail G., Kneib J.-P., Golse G., 2004, A&A, 417, L33
Sousbie T., Pichon C., Colombi S., Novikov D., Pogosyan D., 2008, MNRAS, 383, 1655
Sousbie T., Pichon C., Kawahara H., 2011, MNRAS, 414, 384
Springel V., White S. D. M., Tormen G., Kauffmann G., 2001, MNRAS, 328, 726
Springel V. et al., 2005, Nature, 435, 629
The Dark Energy Survey Collaboration 2005, preprint (arXiv:astro-ph/0510346)
Tormen G., 1998, MNRAS, 297, 648
Tormen G., Moscardini L., Yoshida N., 2004, MNRAS, 350, 1397
Vale C., White M., 2003, ApJ, 592, 699
van den Bosch F. C., Tormen G., Giocoli C., 2005, MNRAS, 359, 1029
Verdugo T., Motta V., Muñoz R. P., Limousin M., Cabanac R., Richard J., 2011, A&A, 527, A124
von der Linden A. et al., 2014, MNRAS, 439, 2
Waizmann J.-C., Redlich M., Bartelmann M., 2012, A&A, 547, A67
Waizmann J.-C., Redlich M., Meneghetti M., Bartelmann M., 2014, A&A, 565, A28
Wang L., Li C., Kauffmann G., De Lucia G., 2006, MNRAS, 371, 537
Wu X.-P., Fang L.-Z., Xu W., 1998, A&A, 338, 813
Xu B. et al., 2016, ApJ, 817, 85
Zhang Y. et al., 2016, ApJ, 816, 98
Zhao D. H., Jing Y. P., Mo H. J., Bnörner G., 2009, ApJ, 707, 354
Zitrin A., Broadhurst T., 2009, ApJ, 703, L132
Zitrin A. et al., 2009, MNRAS, 396, 1985
Zitrin A., Broadhurst T., Barkana R., Rephaeli Y., Benítez N., 2011, MNRAS, 410, 1939
Zitrin A., Broadhurst T., Bartelmann M., Rephaeli Y., Oguri M., Benítez N., Hao J., Umetsu K., 2012, MNRAS, 423, 2308
Zitrin A. et al., 2014, ApJ, 793, L12

This paper has been typeset from a TEX/LATEX file prepared by the author.